Phonon-Assisted Auger-Meitner Recombination in Silicon from First Principles

Kyle Bushick and Emmanouil Kioupakis*
Department of Materials Science and Engineering, University of Michigan, Ann Arbor, Michigan 48109, USA

(Received 17 July 2022; accepted 10 July 2023; published 15 August 2023)

We present a consistent first-principles methodology to study both direct and phonon-assisted Auger-Meitner recombination (AMR) in indirect-gap semiconductors that we apply to investigate the microscopic origin of AMR processes in silicon. Our results are in excellent agreement with experimental measurements and show that phonon-assisted contributions dominate the recombination rate in both n-type and p-type silicon, demonstrating the critical role of phonons in enabling AMR. We also decompose the overall rates into contributions from specific phonons and electronic valleys to further elucidate the microscopic origins of AMR. Our results highlight potential pathways to modify the AMR rate in silicon via strain engineering.

DOI: 10.1103/PhysRevLett.131.076902

Auger-Meitner recombination (AMR), also referred to as Auger recombination in the literature, is an intrinsic nonradiative carrier recombination process in semiconductors that is named after Lise Meitner and Pierre Auger. AMR of free carriers in bulk materials parallels the atomic effect, whereby a core hole is filled by an electron, transferring the excess energy to a second, ejected electron. This atomic emission process was first discovered by Meitner in 1922, and independently by Auger in 1923, bearing both their names in recognition of their contributions [1]. In the semiconductor AMR process, an electron and a hole recombine across the band gap, transferring their energy via the Coulomb interaction to another electron (*eeh* process) or hole (*hhe* process) and exciting it to a high energy state. The AMR mechanism can occur in a direct fashion if the carriers can satisfy both energy and momentum conservation [Fig. 1(a)]. Alternatively, phonon-assisted AMR occurs when momentum conservation is satisfied through the absorption or emission of a phonon [Fig. 1(b)], much like phonon-assisted optical absorption in indirect-gap materials. The additional momentum provided by the phonon increases the number of final electronic states accessible to AMR, making the phonon-assisted process dominant in cases where direct AMR is weak or not possible. The AMR rate for nondegenerate free carriers is proportional to the third power of n ($R = [dN/dt] = CVn^3$), where $n = [N/V]$ is the number of free carriers N per volume V, and C is the AMR coefficient. AMR is of broad interest as it has been shown to limit the maximum efficiency of solar cells [2,3], LEDs [4], bipolar transistors [5], lasers [6,7], the ideality factor in diodes [8], and becomes the dominant recombination pathway at high carrier concentrations.

Despite its scientific and engineering importance, direct and phonon-assisted AMR remains poorly understood in materials—including silicon. While there have been a number of experimental studies and parametrizations of the overall AMR rate in silicon [9–12], important fundamental questions about the process remain unanswered. For one, empirical models rely on challenging measurements and empirical function fits, preventing them from probing the underlying atomistic mechanisms. For example, empirical models are not capable of separating the effects of the different varieties of AMR (e.g., direct or phonon-assisted) or evaluating different microscopic contributions (e.g., from different electron valleys or specific phonon modes). These aspects limit the utility of such models in gaining a fundamental understanding of AMR in silicon.

Considering the constraints of empirical fits to experimental data, theoretical calculations offer an alternative route to probe the underlying mechanisms of AMR. However, past work in this area has been limited by a variety of shortcomings. Early efforts from Huldt investigated the

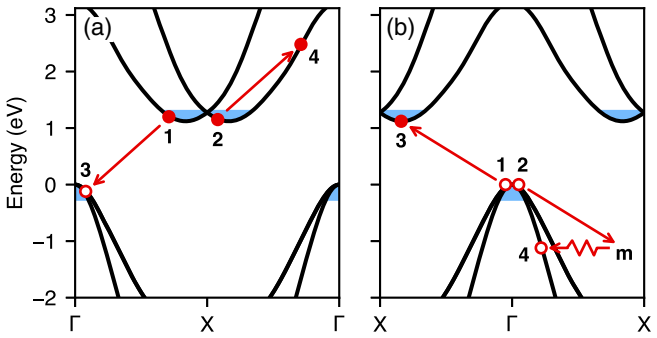

FIG. 1. Quasiparticle band structure of silicon depicting Auger-Meitner recombination processes. (a) Schematic of the direct *eeh* Auger-Meitner process involving two electrons (solid circles) near the conduction band minimum and a hole (open circle) near the valence band maximum. The blue areas indicate the range of initial carrier states that are included in the calculations. (b) Schematic of the phonon-assisted *hhe* Auger-Meitner process, where the inclusion of a phonon conserves the overall momentum and allows this process to take place.

direct AMR process but used a number of approximations to both the band structure and matrix elements, leading to underestimates of the AMR rate [13]. In follow-up work, Lochmann and Haug also considered phonon-assisted processes, but used a semi-empirical band structure, limited the electron-phonon scattering mechanisms and recombination pathways, estimated the matrix elements with $k \cdot p$, and omitted umklapp scattering [14–16]. These simplifications exclude key components of the physical process and can lead to inaccurate results—a finding discussed in greater detail by Laks *et al.* [17,18]. In their subsequent work on direct AMR, Laks *et al.* used an empirical pseudopotential and discarded the previous simplifying assumptions, concluding that the direct AMR process is dominant for *eeh* AMR, though it is insufficient to describe the *hhe* AMR rate. Govoni *et al.* later performed the only first-principles calculation for direct AMR in silicon, finding loose agreement with experimental results for *eeh* AMR and attributing the difference to phonon-assisted AMR [19]. To date, there has not been a full band structure calculation that includes both direct and phonon-assisted processes, a limit imposed by the computational complexity of the problem. This shortcoming has precluded definitive conclusions regarding the microscopic mechanisms of AMR in silicon that are resolved by our Letter.

In this Letter, we implement a consistent first-principles computational methodology to investigate both direct and phonon-assisted AMR in indirect-gap materials at the same level of theory and apply it to address the long-standing challenge of gaining a complete and accurate mechanistic understanding of AMR in silicon. Our results show excellent agreement with experiment, including both the carrier and temperature dependence of the AMR coefficient in this technologically important material. We demonstrate that the phonon-assisted mechanism is dominant, not only for *p*-type silicon, but also for *n*-type silicon, for which direct AMR is also possible. Furthermore, we probe the electron-valley dependence for the direct and phonon-assisted *eeh* processes, and we propose epitaxial strain as a new route for modulating the AMR rate in silicon. Our methodology for accurately assessing both direct and phonon-assisted AMR processes can also be readily applied to other material systems and advance our atomistic understanding of AMR in electronic and optoelectronic semiconductor devices.

The direct AMR coefficient can be evaluated using first-order perturbation theory and Fermi's golden rule, while the phonon-assisted AMR process requires second-order perturbation theory. We direct the reader to Ref. [20] for these formulations, which we also summarize in the Supplemental Material (including Ref. [21]) [22]. The summation in Eq. S2 is computationally intractable if we account for the carrier distribution around the band extrema, as depicted in Fig. 1(b), as the additional momentum of the phonon relaxes the momentum conservation constraint [22]. Thus, to enable the calculation of the phonon-assisted AMR rate, we assume that all low-energy carriers have the energy, momentum, and wave function of the states at the corresponding band extrema. For indirect gap materials, however, care must be taken to deal with the band and valley degeneracies properly. We can rewrite Eq. S2 [22] as

$$R_{pa,eeh} = 2\frac{2\pi n_e^2 n_h}{8\hbar N_{\mathbb{C}}^2 N_{\mathbb{V}}} \sum_{\mathbf{1234};\nu\mathbf{q}} \left(n_{\nu\mathbf{q}} + \frac{1}{2} \pm \frac{1}{2} \right) \times |\tilde{M}_{\mathbf{1234};\nu\mathbf{q}}|^2 \delta(\epsilon_{\mathbf{1}} + \epsilon_{\mathbf{2}} - \epsilon_{\mathbf{3}} - \epsilon_{\mathbf{4}} \mp \hbar\omega_{\nu\mathbf{q}}), \quad (1)$$

for the *eeh* process, where n_e and n_h are the electron and hole carrier concentrations, $N_{\mathbb{C}}$ is the conduction band minimum total degeneracy, defined as $N_{\mathbb{C}} \equiv N^{\mathbb{C}}_{\text{valley}} \times N^{\mathbb{C}}_{\text{band}}$, and $N_{\mathbb{V}}$ is the valence band maximum total degeneracy, defined as $N_{\mathbb{V}} \equiv N^{\mathbb{V}}_{\text{valley}} \times N^{\mathbb{V}}_{\text{band}}$. The $R_{pa,hhe}$ term simply swaps the powers of $N_{\mathbb{C}}$ and n_e with $N_{\mathbb{V}}$ and n_h in the prefactor. For silicon, $N^{\mathbb{C}}_{\text{valley}} = 6$, $N^{\mathbb{C}}_{\text{band}} = 1$, $N^{\mathbb{V}}_{\text{valley}} = 1$, and $N^{\mathbb{V}}_{\text{band}} = 3$. We note that $N^{\mathbb{V}}_{\text{band}} = 3$ because we do not consider spin-orbit coupling in our calculations. Previous work on AMR in InAs found that including spin-orbit coupling did not appreciably alter the AMR rate unless the splitting was large enough to form resonant states with the band gap [23]. Given that the spin-orbit splitting in silicon is significantly smaller than the band gap, we can safely omit it from our calculations in order to reduce the computational cost without suffering any severe loss of accuracy.

We perform our calculations using a range of first-principles tools. We utilize the open-source QUANTUM ESPRESSO package to obtain density functional theory (DFT) wave functions and eigenvalues for the DFT relaxed structure ($a = 5.379$ Å) as well as density functional perturbation theory (DFPT) calculations to obtain the electron-phonon coupling matrix elements [24,25]. We also employ the BERKELEYGW code to calculate the G_0W_0 (GW) quasiparticle corrections to DFT eigenenergies and band curvature [26,27]. Since AMR must be calculated on much finer grids than are required for the band structure, we employ the maximally localized Wannier function method and the WANNIER90 package to interpolate our GW eigenvalues onto arbitrarily fine grids [28]. It is known that even these higher levels of theory do not recover the exact effective masses [29], so we also conduct sensitivity tests of the effective mass on the AMR coefficient, finding that even 10% changes to the effective mass do not appreciably affect the results. While the GW band gap is sensitive to temperature, we show that the AMR coefficient is not strongly dependent on the band gap and therefore do not include these temperature effects in our calculations. Convergence testing with respect to the Brillouin zone (BZ) sampling also demonstrates that our AMR rates are converged within 5% for the direct *eeh* process and both phonon-assisted processes and 11% for

TABLE I. Comparison of calculated and measured AMR coefficients. All data are shown in units of $\times 10^{-31}$ cm^6 s^{-1} at a temperature of 300 K and carrier concentrations in the range of 10^{18} cm^{-3}.

Source	$C_{eeh,dir}$	$C_{eeh,pa}$	$C_{eeh,tot}$	$C_{hhe,dir}$	$C_{hhe,pa}$	$C_{hhe,tot}$
This Letter	0.86	2.33	3.19	0.000089	2.0	2.0
Govoni, Marri, and Ossicini (theory) [19]	~1.07	...	...	~0.000049	...	...
Laks, Neumark, and Pantelides (theory) [18]	~3.9	...	...	~0.015	...	...
Dziewior and Schmid (experiment) [34]	...	...	2.8	...	...	0.99
Häcker and Hangleiter (experiment) [35]	...	...	4.35	...	...	2.02

the direct *hhe* process (which we show to be negligible). Details on these tests, as well as the other computational parameters and their convergence can be found in the Supplemental Material [22], which includes Refs. [30–33].

The summary of our combined direct and phonon-assisted AMR coefficients in silicon are shown in Table I. Our direct calculations agree well with the first-principles results from Govoni, Marri, and Ossicini, which are the most accurate calculations of direct AMR in silicon to date [19]. We also find superb agreement with the experimentally measured values from both Dziewior and Schmid and Häcker and Hangleiter [34,35]. Because of the relatively close agreement between past direct *eeh* calculations and experiment, direct AMR has typically been considered sufficient to explain the measurements in *n*-type silicon [17–19]. Contrasting this, our findings not only confirm that phonon-assisted AMR is the dominant mechanism for the *hhe* process (> 99.9% of the total), but also for *eeh* AMR (~73%), demonstrating the importance of phonons to both *eeh* and *hhe* AMR processes in silicon.

The dependence of the direct and phonon-assisted processes on carrier concentration is shown in Fig. 2. Overall, the AMR coefficient remains approximately constant, though it does decrease at high carrier concentrations. This behavior is due to the fact that the Coulomb interaction is short range for direct AMR, but both short- and long-range interactions play a role for phonon-assisted AMR. Thus, the increased screening at higher carrier concentrations affects the phonon-assisted rate more strongly. On the other hand, at lower carrier concentrations weaker screening enables electron-hole interactions to increase the local carrier concentrations of holes (electrons) around electrons (holes), and therefore increase the rate of AMR recombination, an effect known as Coulomb enhancement [9,11,36]. Including these many-body effects is outside the scope of our Letter, but Hangleiter and Häcker and Richter *et al.* have developed Coulomb-enhancement factors which we apply to our results in Fig. 2 to estimate such effects [11,36]. We see that both correction factors recover the correct trend, validating that Coulomb-enhancement is responsible for the discrepancy between our calculations and measurements at lower carrier concentrations. At higher carrier concentrations, increased screening neutralizes the Coulomb-enhancement effects. We provide a physically informed model for $C(n, p)$ in the Supplemental Material [22], including Refs. [37] and [38].

We also examined the effect of temperature on the direct and phonon-assisted processes at a fixed carrier concentration of 10^{18} cm^{-3} (Fig. 3). We find that temperature has a negligible effect on the direct AMR coefficient but the phonon-assisted process is more sensitive to temperature and follows the Bose-Einstein distribution, indicating that an increasing phonon population is the primary driver of this temperature dependence. While there is sparse experimental data investigating the temperature dependence of AMR at these carrier concentrations, we do find reasonable agreement between our calculations and the range of available experiments. We also formulate a physically motivated parameterization for $C(T)$, which is discussed in the Supplemental Material [22] and includes Ref. [39].

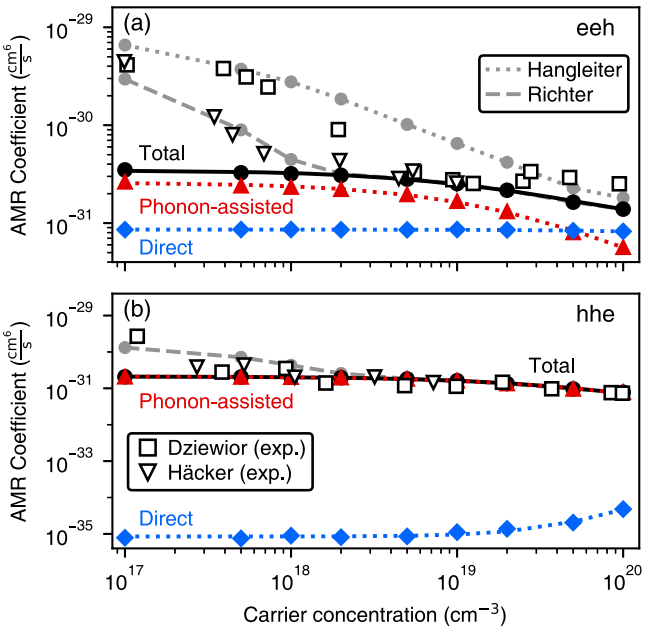

FIG. 2. AMR coefficient (C) as a function of carrier concentration for (a) the *eeh* process and (b) the *hhe* process at 300 K. We decompose the total rate (black circles) into contributions from the phonon-assisted (red triangles) and direct (blue diamonds) processes. The curves are generated by our model [Eq. S4] [22]. We also compare our results to experimental measurements [34,35] and approximate Coulomb-enhancement effects using existing models [11,36].

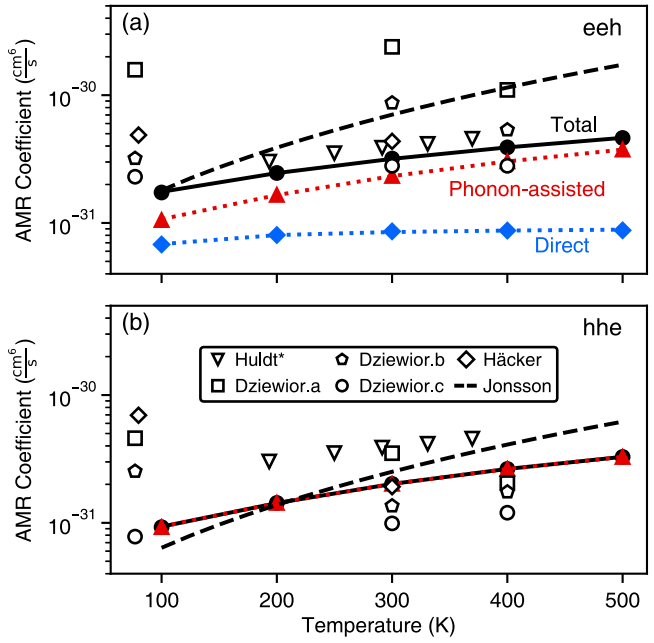

FIG. 3. AMR coefficient as a function of temperature for (a) the *eeh* process and (b) the *hhe* process at a carrier concentration of 10^{18} cm^{-3}. We decompose the total rate (black circles) into contributions from the phonon-assisted (red triangles) and direct (blue diamonds) processes. The curves are generated by our model [Eq. S5] [22]. Experimental data points are also included for comparison, though we note that not all points are at carrier concentrations of exactly 10^{18} cm^{-3} [34,35,40,41].

By leveraging our first-principles methodology we are able to decompose the overall AMR rate into distinct valley and phonon contributions. In the *eeh* process, there are three unique possibilities for the starting valley arrangements of the participating electrons: both electrons originating in the same valley (intravalley), electrons originating in opposite valleys (g-type), or electrons originating in perpendicular valleys (f-type), shown in Fig. 4(b) (although we follow the same notation as phonon-scattering processes, we emphasize that these descriptions do not refer to scattering but rather to the initial valley arrangement of the two electrons during *eeh* AMR). The f-type and intravalley terms are nearly equal for direct *eeh* AMR (with negligible g-type contribution), consistent with the findings of Laks *et al.* [18], while the f-type arrangement dominates for phonon-assisted recombination, and therefore for the overall rate [Fig. 4(a)]. This finding demonstrates a pathway for modulating the AMR rate via strain engineering: applying biaxial strain changes the relative energies of the different conduction band valleys and therefore the distribution of electrons, tuning the viability of different valley arrangements. Indeed, using strain to modulate the carrier occupation in bulk semiconductors is a technique that has been applied to engineer a variety of material properties, including the carrier mobility [42–44].

We also investigate phonon-assisted AMR as a function of the participating phonon energies and momenta. Decomposing the total coefficient by phonon frequency

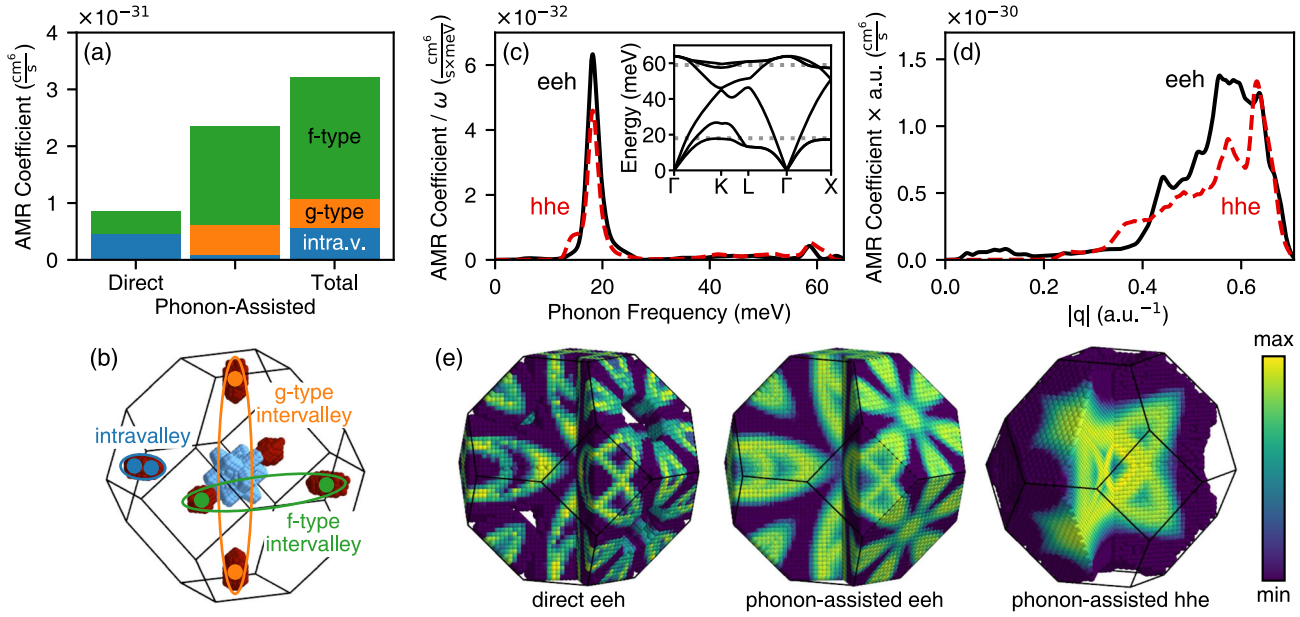

FIG. 4. Analysis of different contributions to the overall AMR rate. (a) Relative importance of the three different initial valley arrangements for electrons in the *eeh* process, which are illustrated in (b) with the f-type arrangement contributing most strongly. The strength of phonon-assisted AMR for *eeh* (solid black) and *hhe* (red dash) processes as a function of phonon energy (c) and wave vector magnitude (d), where the strongest peaks are associated with TA phonons, highlighted in the inset phonon dispersion. (e) The distribution of excited carrier states throughout the first Brillioun zone for the direct and phonon-assisted *eeh* and phonon-assisted *hhe* processes, with slices removed to show the internal structure.

[Fig. 4(c)], we observe two distinct peaks around 18 (short wavelength TA modes) and 59 meV (primarily TO modes). The peak at 18 meV accounts for ∼78% of the *eeh* and ∼66% of the *hhe* AMR coefficient. These fractions indicate that while phonons across the energy spectrum play a role in phonon-assisted AMR, the zone-edge acoustic phonons dominate. Furthermore, the phonon emission process accounts for the majority of both *eeh* (74%) and *hhe* (67%) phonon-assisted AMR processes, indicating that it is not possible to freeze out the phonon-assisted AMR mechanism in silicon even at cryogenic temperatures. We also analyze the contributions of different phonon wave vectors to the overall phonon-assisted AMR rate [Fig. 4(d)]. We observe that at long wavelengths ($|q| < 0.2$ a.u.$^{-1}$) *hhe* phonon-assisted AMR is forbidden (by momentum conservation) while *eeh* phonon-assisted AMR is extremely weak (only 3% of the total). This result justifies approximating the carrier wave function of wave vector $\mathbf{k}$ by those at the nearest band extrema, as any small deviations from the band extrema are negligible compared to the large wave vectors $\mathbf{q}$ that dominate the phonon-assisted AMR process. Further analysis and visualization of the contributing phonon modes are found in the Supplemental Material [22].

Finally, we examine the distribution of the final states of excited electrons and holes. Plotting this distribution over the BZ provides a clear example of why the phonon-assisted process is important in *eeh* AMR. The distributions of the direct and phonon-assisted processes are nearly identical [Fig. 4(e)], with the exception being states near the L point. These states contribute strongly to the overall AMR rate yet are inaccessible without the additional momentum provided by phonons. While the excited hole isosurface has similar topology to the hole Fermi surface [as in Fig. 4(b)], there are also new features that emerge that are unique to the high-energy holes, such as the lobes towards the L points. In both *eeh* and *hhe* cases, this analysis also illustrates the large momentum transfer occurring in the Coulomb interaction, which reinforces the need for our first-principles atomistic treatment of AMR as methods such as $k \cdot p$ do not describe the bands accurately far from the band extrema.

In summary, we investigated the direct and phonon-assisted AMR rate in silicon from first principles. Our calculations are in excellent agreement with experimental values and demonstrate the importance of the phonon-assisted AMR process in both n-type (*eeh* dominant) and p-type (*hhe* dominant) silicon, answering the long-standing question about the role of phonons in AMR in silicon. Our analysis shows that short wavelength phonons (primarily acoustic) dominate the phonon-assisted AMR mechanism. The large momentum transfer involved in both the Coulomb and electron-phonon scattering processes underscores the need for a first-principles atomistic treatment of AMR in silicon. We further propose a potential pathway for modulating the AMR rate by tuning the carrier occupations of different conduction band valleys via strain engineering. Our methodology elucidates the microscopic origins of AMR in silicon and paves the way for unprecedented scientific understanding and engineering of this fundamental recombination mechanism in other technologically important direct- and indirect-gap semiconductors.

We thank Chris Van de Walle and David Young for helpful discussions. The work is supported as part of the Computational Materials Sciences Program funded by the U.S. Department of Energy, Office of Science, Basic Energy Sciences under Award No. DE-SC0020129. This work used resources of the National Energy Research Scientific Computing (NERSC) Center, a DOE Office of Science User Facility supported under Contract No. DE-AC02–05CH11231. K. B. acknowledges the support of the U.S. Department of Energy, Office of Science, Office of Advanced Scientific Computing Research, Department of Energy Computational Science Graduate Fellowship under Award No. DE-SC0020347.

*kioup@umich.edu

[1] D. Matsakis, A. Coster, B. Laster, and R. Sime, A renaming proposal: "The Auger–Meitner effect", Phys. Today **72**, No. 9, 10 (2019).
[2] T. Tiedje, E. Yablonovitch, G. Cody, and B. Brooks, Limiting efficiency of silicon solar cells, IEEE Trans. Electron Devices **31**, 711 (1984).
[3] M. J. Kerr, A. Cuevas, and P. Campbell, Limiting efficiency of crystalline silicon solar cells due to Coulomb-enhanced Auger recombination, Prog. Photovoltaics **11**, 97 (2003).
[4] Y. C. Shen, G. O. Mueller, S. Watanabe, N. F. Gardner, A. Munkholm, and M. R. Krames, Auger recombination in InGaN measured by photoluminescence, Appl. Phys. Lett. **91**, 141101 (2007).
[5] M. Tyagi and R. Van Overstraeten, Minority carrier recombination in heavily-doped silicon, Solid-State Electron. **26**, 577 (1983).
[6] M. Takeshima, Effect of Auger recombination on laser operation in $Ga_{1-x}Al_xAs$, J. Appl. Phys. **58**, 3846 (1985).
[7] J. Singh, *Semiconductor Optoelectronics: Physics and Technology*, 1st ed. (McGraw-Hill College, New York, 1995).
[8] M. Leilaeioun and Z. C. Holman, Accuracy of expressions for the fill factor of a solar cell in terms of open-circuit voltage and ideality factor, J. Appl. Phys. **120**, 123111 (2016).
[9] P. P. Altermatt, J. Schmidt, G. Heiser, and A. G. Aberle, Assessment and parameterisation of Coulomb-enhanced Auger recombination coefficients in lowly injected crystalline silicon, J. Appl. Phys. **82**, 4938 (1997).
[10] M. J. Kerr and A. Cuevas, General parameterization of Auger recombination in crystalline silicon, J. Appl. Phys. **91**, 2473 (2002).
[11] A. Richter, S. W. Glunz, F. Werner, J. Schmidt, and A. Cuevas, Improved quantitative description of Auger

recombination in crystalline silicon, Phys. Rev. B **86**, 165202 (2012).
[12] L. E. Black and D. H. Macdonald, On the quantification of Auger recombination in crystalline silicon, Sol. Energy Mater. Sol. Cells **234**, 111428 (2022).
[13] L. Huldt, Band-to-band auger recombination in indirect gap semiconductors, Phys. Status Solidi (a) **8**, 173 (1971).
[14] W. Lochmann, Phonon-assisted auger recombination in indirect gap semiconductors, Phys. Status Solidi (a) **45**, 423 (1978).
[15] A. Haug, Auger coefficients for highly doped and highly excited semiconductors, Solid State Commun. **28**, 291 (1978).
[16] W. Lochmann and A. Haug, Phonon-assisted Auger recombination in Si with direct calculation of the overlap integrals, Solid State Commun. **35**, 553 (1980).
[17] D. B. Laks, G. F. Neumark, A. Hangleiter, and S. T. Pantelides, Theory of Interband Auger Recombination in *n*-type Silicon, Phys. Rev. Lett. **61**, 1229 (1988).
[18] D. B. Laks, G. F. Neumark, and S. T. Pantelides, Accurate interband-Auger-recombination rates in silicon, Phys. Rev. B **42**, 5176 (1990).
[19] M. Govoni, I. Marri, and S. Ossicini, Auger recombination in Si and GaAs semiconductors: *Ab initio* results, Phys. Rev. B **84**, 075215 (2011).
[20] E. Kioupakis, D. Steiauf, P. Rinke, K. T. Delaney, and C. G. Van de Walle, First-principles calculations of indirect Auger recombination in nitride semiconductors, Phys. Rev. B **92**, 035207 (2015).
[21] G. Cappellini, R. Del Sole, L. Reining, and F. Bechstedt, Model dielectric function for semiconductors, Phys. Rev. B **47**, 9892 (1993).
[22] See Supplemental Material at http://link.aps.org/supplemental/10.1103/PhysRevLett.131.076902 for discussion of the perturbation theory formulation, details related to convergence and parameter selection, physically informed models of the AMR coefficient, and additional visualization.
[23] J.-X. Shen, D. Steiauf, A. McAllister, G. Shi, E. Kioupakis, A. Janotti, and C. G. Van de Walle, Impact of phonons and spin-orbit coupling on Auger recombination in InAs, Phys. Rev. B **100**, 155202 (2019).
[24] P. Giannozzi *et al.*, QUANTUM ESPRESSO: A modular and open-source software project for quantum simulations of materials, J. Phys. Condens. Matter **21**, 395502 (2009).
[25] P. Giannozzi *et al.*, Advanced capabilities for materials modelling with QUANTUM ESPRESSO, J. Phys. Condens. Matter **29**, 465901 (2017).
[26] M. S. Hybertsen and S. G. Louie, Electron correlation in semiconductors and insulators: Band gaps and quasiparticle energies, Phys. Rev. B **34**, 5390 (1986).
[27] J. Deslippe, G. Samsonidze, D. A. Strubbe, M. Jain, M. L. Cohen, and S. G. Louie, BERKELEYGW: A massively parallel computer package for the calculation of the quasiparticle and optical properties of materials and nanostructures, Comput. Phys. Commun. **183**, 1269 (2012).
[28] G. Pizzi *et al.*, WANNIER90 as a community code: new features and applications, J. Phys. Condens. Matter **32**, 165902 (2020).
[29] S. Poncé, E. R. Margine, and F. Giustino, Towards predictive many-body calculations of phonon-limited carrier mobilities in semiconductors, Phys. Rev. B **97**, 121201(R) (2018).
[30] Y. Okada and Y. Tokumaru, Precise determination of lattice parameter and thermal expansion coefficient of silicon between 300 and 1500 K, J. Appl. Phys. **56**, 314 (1984).
[31] J. Deslippe, G. Samsonidze, M. Jain, M. L. Cohen, and S. G. Louie, Coulomb-hole summations and energies for *GW* calculations with limited number of empty orbitals: A modified static remainder approach, Phys. Rev. B **87**, 165124 (2013).
[32] W. Bludau, A. Onton, and W. Heinke, Temperature dependence of the band gap of silicon, J. Appl. Phys. **45**, 1846 (1974).
[33] A. M. Brown, R. Sundararaman, P. Narang, W. A. Goddard, and H. A. Atwater, Nonradiative plasmon decay and hot carrier dynamics: Effects of phonons, surfaces, and geometry, ACS Nano **10**, 957 (2016).
[34] J. Dziewior and W. Schmid, Auger coefficients for highly doped and highly excited silicon, Appl. Phys. Lett. **31**, 346 (1977).
[35] R. Häcker and A. Hangleiter, Intrinsic upper limits of the carrier lifetime in silicon, J. Appl. Phys. **75**, 7570 (1994).
[36] A. Hangleiter and R. Häcker, Enhancement of Band-to-Band Auger Recombination by Electron-Hole Correlations, Phys. Rev. Lett. **65**, 215 (1990).
[37] A. David and M. J. Grundmann, Droop in InGaN light-emitting diodes: A differential carrier lifetime analysis, Appl. Phys. Lett. **96**, 103504 (2010).
[38] A. McAllister, D. Bayerl, and E. Kioupakis, Radiative and Auger recombination processes in indium nitride, Appl. Phys. Lett. **112**, 251108 (2018).
[39] A. McAllister, D. Åberg, A. Schleife, and E. Kioupakis, Auger recombination in sodium-iodide scintillators from first principles, Appl. Phys. Lett. **106**, 141901 (2015).
[40] L. Huldt, N. G. Nilsson, and K. G. Svantesson, The temperature dependence of band-to-band Auger recombination in silicon, Appl. Phys. Lett. **35**, 776 (1979).
[41] P. Jonsson, H. Bleichner, M. Isberg, and E. Nordlander, The ambipolar Auger coefficient: Measured temperature dependence in electron irradiated and highly injected n-type silicon, J. Appl. Phys. **81**, 2256 (1997).
[42] D. Yu, Y. Zhang, and F. Liu, First-principles study of electronic properties of biaxially strained silicon: Effects on charge carrier mobility, Phys. Rev. B **78**, 245204 (2008).
[43] K. Bushick, S. Chae, Z. Deng, J. T. Heron, and E. Kioupakis, Boron arsenide heterostructures: lattice-matched heterointerfaces and strain effects on band alignments and mobility, npj Comput. Mater. **6**, 3 (2020).
[44] S. Poncé, D. Jena, and F. Giustino, Route to High Hole Mobility in GaN via Reversal of Crystal-Field Splitting, Phys. Rev. Lett. **123**, 096602 (2019).